23rd ABCM International Congress of Mechanical Engineering
December 6-11, 2015, Rio de Janeiro, RJ, Brazil

TURBULENT 3D LID-DRIVEN CAVITY FLOW OF VISCOPLASTIC FLUIDS

Paulo Arthur Beck
Horácio Antonio Vielmo
Sérgio L. Frey
Department of Mechanical Engineering, Federal University of Rio Grande do Sul (UFRGS), Rua Sarmento Leite 425, 90050-170, Porto Alegre, RS, Brazil
paulo.beck@ufrgs.br, vielmoh@mecanica.ufrgs.br, frey@mecanica.ufrgs.br

Abstract. *The authors investigate the turbulent 3D lid-driven cavity flow of viscoplastic fluids, aiming to validate the application of the Reynolds Stress Transport turbulence model coupled with a regularized viscosity function. For that, the SMD viscosity function and the Navier-Stokes equations are solved together with the transport equations of the turbulence model. The Finite-Volume Method is used to approximate the resulting system of equations which are solved using the code STAR-CCM+. The analysis of the viscoplasticity and inertia effects uses dimensionless flow and rheological quantities, and the state of turbulence assessment relies on the mapping of the anisotropy of the Reynolds stresses. The combined effects of flow inertia and fluid rheology are discussed, and the state of turbulence and velocity profiles are determined for mildly and fully turbulent flows. Moreover, considerations are drawn concerning the applicability and stability of the numerical solution in the limiting case of substantial non-linearity of the viscosity function. The results demonstrate the rheology of the fluids markedly influences the state of turbulence, and the return-to-isotropy trajectories of the Reynolds stresses. In conclusion, the coupling of the Reynolds Stress Transport turbulence model and a regularized viscosity function produces consistent results from both rheological and turbulence perspectives.*

Keywords: *viscoplastic fluids, SMD viscosity function, lid-driven cavity flow, turbulence.*

1. INTRODUCTION

Viscoplastic fluids are a class of inelastic materials that need to exceed a rheological stress level (the yield-stress limit) to start flowing. If the internal stress level is below such a limit, the material has high viscosity, either experiencing low deformations or performing a rigid body motion in (apparently) unyielded regions. At the yield stress, the material structure breaks and starts flowing at much lower viscosity levels (yielded regions). Early models describing viscoplasticity (Bird, 1982) are the Bingham plastic (the material flows as a Newtonian fluid when the shear stress exceeds the yield-stress limit) and the Herschel–Bulkley (the viscosity of the material decreases nonlinearly as the strain-rate increases after the yield-stress limit). Although widely used, those models fail to describe the behavior of actual viscoplastic fluids by predicting infinite viscosities and no deformation at low strain-rates. Additionally, two equations are required to describe the yielded and unyielded regions, such fact causing discontinuities when one contemplates a numerical solution for a viscoplastic fluid flow. One approach to circumvent those difficulties is to using the augmented Lagrangian method (Huigol and Hou, 2005), which incorporates the effects of the yield stress along with the purely viscous aspects by combining the constitutive relation and the equations of motion into one set of equations. However, for the sake of easily implementing custom code in the solver, the authors adopted the single, regularized and continuous viscosity function proposed by de Souza Mendes and Dutra (2004), herein called the SMD model.

Turbulent flows of viscoplastic fluids occur in bifurcations of the vascular system, sewage transport, drilling, and aseptic food processing among other situations. Most of the papers in the literature focus on viscoelastic fluid flows, due to the drag reducing effect caused by the addition of dilute polymers. Nevertheless, numerical investigations of the turbulent flow of viscoplastic, shear-thinning fluids are scarce because of the lack of models with one or two point closure. Earlier investigations can be found in the papers from Malin (1997,1998) and Cruz et al. (2000), who independently deduced modified $k-\varepsilon$ transport equations for turbulent flows of inelastic power-law fluids. In those models, the apparent viscosity of the flow is the sum of the turbulent eddy viscosity arising from closure of the Reynolds stresses through use of the Boussinesq stress-strain relationship, and the kinematic viscosity of the Herschel-Bulkley fluid. Peixinho et al. (2005) showed that the turbulence intensity is larger for viscoplastic fluid flows, and Rudman and Blackburn (2006) reported results indicating that the yield stress significantly dampens turbulence intensities in the core of the flow where the quasi-laminar flow region co-exists with a transitional wall zone. Gori and Boghi (2012) derived exactly the turbulent dissipation rate equation assuming the viscosity depending only on the second invariant of the strain rate tensor.

In this work, the authors adopt the turbulent, 3D lid-driven cavity flow in order to validate the application of the linear pressure-strain Reynolds Stress Transport (RST) turbulence model of Gibson and Launder (1978). The choice of the cavity flow is justified by the ubiquity of results in the literature (Guia et al., 1982; Chiang et al., 1998; Shankar and Deshpande, 2000), and particularly for viscoplastic fluids, the study reported in dos Santos et al. (2011). The choice of the turbulence model is explained by its ability for accounting effects such as the existence of secondary flows, anisotropy due to strong swirling motion, streamline curvature, and rapid changes in strain-rate. Although it is known that for a given flow condition yield-stress fluids present a higher anisotropy of Reynolds stresses as compared to a Newtonian fluid, and in the near-wall region the state of turbulence is predominantly one-component, the use of the RST turbulence model coupled with a regularized viscosity function present a novel alternative when one considers using a commercially available CFD code to solving turbulent flows of a viscoplastic fluid. Such approach, similar to that reported by Malin (1998) when computing turbulent flows of power-law fluids in smooth circular tubes, introduces the shear-thinning and yield stress effects in the conservation equations by replacing the viscosity with a regularized viscosity function such as that of the SMD model.

2. MATHEMATICAL MODEL

2.1 Conservation equations

The incompressible flow, unsteady state Navier-Stokes transport equations for continuity and momentum, equations (1) and (2) respectively, are used to compute the fluid motion under the assumptions there are no streamwise pressure gradients, and the gravitational effects are unimportant:

$$\frac{d}{dt}\int_V dV + \oint_A \mathbf{u}\cdot\mathbf{da} = 0 \text{ , and} \tag{1}$$

$$\frac{d}{dt}\int_V \mathbf{u}dV + \oint_A \mathbf{u}\otimes\mathbf{u}\cdot\mathbf{da} = 1/\rho \oint_A \mathbf{T}\cdot\mathbf{da} \ . \tag{2}$$

In the preceding equations, ρ is the density, $\mathbf{da}$ is an infinitesimal area vector, dV is an infinitesimal volume, and $\mathbf{u}$ is the velocity vector. In the left-hand side of Eq. (2) are the transient and the advective flux terms, and in the right-hand side is the viscous flux term, where the viscous stress tensor $\mathbf{T} = \mathbf{T}_l + \mathbf{T}_t$ is the sum of the laminar and turbulent stress tensors respectively. The laminar stress tensor is given by

$$\mathbf{T}_l = \mu[\nabla\mathbf{u} + \nabla\mathbf{u}^{\mathrm{T}} - 2/3\,(\nabla\cdot\mathbf{u})\mathbf{I}] \ , \tag{3}$$

where μ is the viscosity (computed with the SMD model as later detailed), and $\mathbf{I}$ is the identity tensor. The turbulent stress tensor $\mathbf{T}_t$, and other turbulent quantities are computed with the transport equations of the linear pressure-strain RST turbulence model, described as follows.

2.2 Linear pressure-strain RST turbulence model

In the linear pressure-strain RST turbulence model of Gibson and Launder (1978), the turbulent stress is defined as

$$\mathbf{T}_t \equiv -\rho\mathbf{R} \ , \tag{4}$$

where $\mathbf{R} \equiv R_{ij} = \overline{u_i u_j}$ is the Reynolds stress tensor. The diagonal components of $\mathbf{R}$ ($\overline{u_1^2}$, $\overline{u_2^2}$, and $\overline{u_3^2}$ in the streamwise, normal, and tangential directions respectively) are normal stresses, while the off-diagonal components (e.g. $\overline{u_1 u_2}$) are shear stresses. The transport equation of the Reynolds stress tensor is

$$\frac{d}{dt}\int_V \mathbf{R}dV + \int_A \mathbf{R}(\mathbf{u}\cdot\mathbf{da}) = 1/\rho\left[\int_A \mathbf{D}\cdot\mathbf{da} + \int_V(\mathbf{P} - 2/3\,\rho\mathbf{I}\varepsilon + \mathbf{\Phi})dV\right] , \tag{5}$$

where the tensor terms in the right-hand side are the turbulent diffusion, turbulent production, isotropic turbulent dissipation rate, and linear pressure-strain. The turbulent diffusion term is computed with

$$\mathbf{D} = (\mu + \mu_t/\sigma_k)\nabla\mathbf{R} \ , \tag{6}$$

where the isotropic turbulent viscosity μ_t is given by

$$\mu_t = \rho C_\mu\, k^2/\varepsilon \ . \tag{7}$$

In the previous equations, $\sigma_k = 0.82$ and $C_\mu = 0.09$ are model coefficients. The turbulent kinetic energy k is obtained directly from the Reynolds stress tensor, and it is defined as

$$k \equiv 1/2\,(tr\,\mathbf{R})\ . \tag{8}$$

The isotropic turbulent dissipation rate ε is obtained from the transport equation

$$\frac{d}{dt}\int_V \varepsilon dV + \int_A \varepsilon\mathbf{u}\cdot\mathbf{da} = 1/\rho\left[\int_A(\mu+\mu_t/\sigma_\varepsilon)\nabla\varepsilon\cdot\mathbf{da} + \int_V[\varepsilon/k\,(C_{\varepsilon1}tr\,\mathbf{P} - C_{\varepsilon2}\rho\varepsilon)]dV\right]\ . \tag{9}$$

In the above equation, $C_{\varepsilon1} = 1.44$, $C_{\varepsilon2} = 1.92$, and $\sigma_\varepsilon = 1.0$ are model coefficients, and the turbulent production tensor is evaluated without recourse to modeling as

$$\mathbf{P} = -\rho(\mathbf{R}\cdot\nabla\mathbf{u}^{\mathrm{T}} + \nabla\mathbf{u}\cdot\mathbf{R})\ . \tag{10}$$

The pressure-strain interactions affect the Reynolds stresses by two different physical processes - first due to pressure fluctuations due to the mutual interaction between turbulent scales and second, the interaction between these regions and those with different average speeds (Launder et al., 1975). In Eq. (5), those interactions are accounted for by the linear pressure-strain tensor term given by

$$\mathbf{\Phi} = \mathbf{\Phi}_s + \mathbf{\Phi}_r + \mathbf{\Phi}_{1w} + \mathbf{\Phi}_{2w}\ , \tag{11}$$

where the four terms are the slow part, the rapid part and their respective wall-reflection terms. The slow pressure-strain term $\mathbf{\Phi}_s$ is modeled as

$$\mathbf{\Phi}_s = -C_1\rho\varepsilon/k[(\mathbf{R} - 2/3k\mathbf{I})]\ , \tag{12}$$

and the rapid pressure-strain term $\mathbf{\Phi}_r$ is modeled as

$$\mathbf{\Phi}_r = -C_2[\mathbf{P} - 1/3\mathbf{I}(tr\,\mathbf{P})]\ . \tag{13}$$

The slow wall-reflection term $\mathbf{\Phi}_{1w}$ is modeled as

$$\mathbf{\Phi}_{1w} = \rho C_{1w}(\varepsilon/k)[(\mathbf{R}{:}\mathbf{N})\mathbf{I} - 3/2\,(\mathbf{R}\cdot\mathbf{N} + \mathbf{N}\cdot\mathbf{R})]f_w\ , \tag{14}$$

where $f_w = \min(k^{3/2}/C_l\mu y, f_w^{\max})$, $f_w^{\max} = 1.4$, and $\mathbf{N} = \mathbf{n}\otimes\mathbf{n}$, with the wall-normal unit vector $\mathbf{n}$ defined as the negative of the wall direction. The rapid wall-reflection term $\mathbf{\Phi}_{2w}$ is modeled as

$$\mathbf{\Phi}_{2w} = C_{2w}[(\mathbf{\Phi}_r{:}\mathbf{N})\mathbf{I} - 3/2\,(\mathbf{\Phi}_r\cdot\mathbf{N} + \mathbf{N}\cdot\mathbf{\Phi}_r)]f_w\ . \tag{15}$$

The coefficients in equations (11)-(15) evaluate as follows, in terms of the turbulent Reynolds number, defined as a function of the wall distance y as

$$Re_y \equiv \rho\sqrt{k}y/\mu\ , \tag{16}$$

and the (normalized) deviatoric part of the Reynolds stress tensor $A_{ij} = \overline{u_i u_j}/k - 2/3\,\delta_{ij}$:

$$C_1 = 1 + 2.58a(a_2^{1/4})\{1 - exp[(-0.0067Re_y)^2]\}\ , \tag{17}$$

$$C_2 = 0.75\sqrt{a}\ , \tag{18}$$

$$C_{1w} = -2/3\,C_1 + 1.67\ , \text{ and} \tag{19}$$

$$C_{2w} = max[(4C_2 - 1)/6C_2, 0]\ . \tag{20}$$

In the equations above, $a = 1 - 9/8\,(a_2 - a_3)$, $a_2 = A_{ij}A_{ji}$, and $a_3 = A_{ik}A_{kj}A_{ji}$.

2.3 Near-wall treatment

The turbulent kinetic energy is computed with Eq. (8) throughout the domain and down right to the wall, and the near-wall values of the turbulent viscosity and turbulent dissipation rate merge with their respective isotropic values, obtained with Eq. (7) and (9) respectively, by means of a one-equation blending function. In this two-layer approach to solving turbulent quantities (Rodi, 1991), the near-wall turbulent dissipation rate is given by

$$\varepsilon_{wall} = k^{3/2}/l_\varepsilon \ , \tag{21}$$

where l_ε is a length-scale that is computed following the proposition of Wolfstein (1969):

$$l_\varepsilon = c_l y[1 - exp(-Re_y/A_\varepsilon)] \ . \tag{22}$$

In the above equation, $A_\varepsilon = 2c_l$ and $c_l = \kappa C_\mu^{-3/4}$are model coefficients, and $\kappa = 0.42$ is the Kolmogorov constant. The near-wall viscosity is computed with

$$\mu_{t,wall} = \lambda\mu_t + (1-\lambda)\mu(\mu_t/\mu)_{wall} \ , \tag{23}$$

where λ is a blending factor, and $(\mu_t/\mu)_{wall}$ is the near-wall turbulent viscosity ratio which is given by the equation

$$(\mu_t/\mu)_{wall} = Re_y C_\mu^{1/4}\kappa[1 - exp(-Re_y/A_\mu)] \ . \tag{24}$$

The blending factor λ is computed with

$$\lambda = 1/2\{1 + tanh[(Re_y - Re_y^*)/A]\} \ , \tag{25}$$

and in the previous equations, $A_\mu = 70$, $Re_y^* = 60$ and $A = 4.35$ are model coefficients.

2.4 The SMD model

In the SMD model of de Souza Mendes and Dutra (2004), the viscosity μ of the fluid is given by a regularized function of the strain-rate $\dot{\gamma}$, the zero-strain-rate viscosity μ_0 , the infinite-strain-rate viscosity μ_{inf} , the yield-stress τ_0 , the consistency index K, and the power-law index n such that

$$\mu(\dot{\gamma}) = [1 - exp(-\mu_0\dot{\gamma}/\tau_0)](\tau_0/\dot{\gamma} + K\dot{\gamma}^{n-1}) + \mu_{inf}[1 - exp(-\mu_{inf}/K\dot{\gamma}^{n-1})] \ . \tag{26}$$

The strain-rate is obtained by computing the second-invariant of the strain-rate tensor $\mathbf{S} = 1/2(\nabla\mathbf{u} + \nabla\mathbf{u}^T)$ such that

$$\dot{\gamma} = \sqrt{(2tr\,\mathbf{S}^2)} \ . \tag{27}$$

The regularization terms (between the square brackets) control both the yield stress and the power-law terms of the viscosity function, and in the limiting situation of zero strain-rate, the viscosity value smoothly departs from μ_0 and tends to μ_{inf} as the strain-rate increases. This behavior can be observed in Fig. 1, which plots Eq. (26) for $K = 1$ Pa·s^n, $n = 0.65$, $\mu_0 = 1$E4 Pa·s, $\mu_{inf} = 1$E-3 Pa·s, and $\tau_0 = 1$ N/m^2. In this figure, the strain-rate value for which the viscosity function drops from the Newtonian plateau is defined as $\dot{\gamma}_0 \equiv \tau_0/\mu_0$, and the strain-rate range between $\dot{\gamma}_1 \equiv (\tau_0/K)^{1/n}$ and $\dot{\gamma}_2 \equiv (K/\mu_{inf})^{1/(1-n)}$ defines the power-law region (de Souza Mendes, 2007).

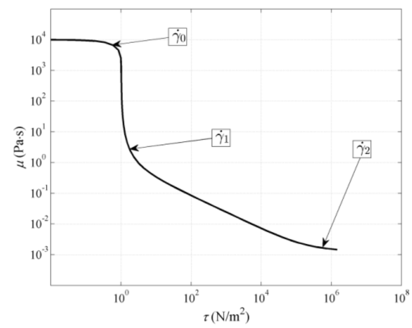

Figure 1. Plot of Eq. (26) for $K = 1$ Pa·s^n, $n = 0.65$, $\mu_0 = 1$E4 Pa·s, $\mu_{inf} = 1$E-3 Pa·s, and $\tau_0 = 1$ N/m^2

3. NUMERICAL METHOD

3.1 The Finite-Volume method

The Finite-Volume method (Patankar, 1980) is adopted to approximate the transport equations of the mathematical model. In this method, the transport equation of a scalar ϕ for a control volume V centered on cell-0 is

$$\frac{d}{dt}(\rho\phi V)_0 + \sum_f \rho\phi(\mathbf{u}\cdot\mathbf{a})_f = \sum_f(\Gamma\nabla\phi\cdot\mathbf{a})_f \ , \tag{28}$$

where $\mathbf{u}$ is the velocity vector through a cell-face f, $\mathbf{a}$ is the area vector of cell-face f, and Γ is the diffusivity. The transient term in Eq. (28) is approximated by the Euler Implicit (first-order) temporal scheme as follows:

$$\frac{d}{dt}(\rho\phi V)_0 = [(\rho_0\phi_0)^{i+1} - (\rho_0\phi_0)^i]/\Delta t\, V_0. \tag{29}$$

In the previous equation, i denotes the time-step and the advective term at the cell-face f is approximated with

$$\frac{d}{dt}(\rho\phi V)_0 = [(\rho_0\phi_0)^{i+1} - (\rho_0\phi_0)^i]/\Delta t\, V_0 \ , \tag{30}$$

and the advective term at cell-face f is given by

$$\rho\phi(\mathbf{u}\cdot\mathbf{a})_f = (\dot{m}\phi)_f = \dot{m}_f\phi_f \tag{31}$$

where $\dot{m}_f$ and ϕ_f are the mass flow rates and scalar values at the face respectively. For a second-order upwind scheme, the advective flux is obtained with

$$(\dot{m}\phi)_f = \dot{m}_f\phi_{f,0} \text{ for } \dot{m}_f \geq 0 \text{ , and} \tag{32}$$

$$(\dot{m}\phi)_f = \dot{m}_f\phi_{f,1} \text{ for } \dot{m}_f < 0 \ . \tag{33}$$

In the previous equations, the face values $\phi_{f,0}$ and $\phi_{f,1}$ are linearly interpolated from the cell values on either side of the face with

$$\phi_{f,0} = \phi_0 + \mathbf{s}_0\cdot(\nabla\phi)_0 \text{ , and} \tag{34}$$

$$\phi_{f,1} = \phi_1 + \mathbf{s}_1\cdot(\nabla\phi)_1 \ . \tag{35}$$

The gradients of the scalar ϕ at face f of cells-0 and 1 are $(\nabla\phi)_0$ and $(\nabla\phi)_1$ respectively, and $\mathbf{s}_0$ and $\mathbf{s}_1$ are the distance vectors between the centroids and the faces of the cells. The Hybrid Gauss-Least Squares Method, and the Venkatakrishnan limiter (1993) are used to compute gradients of field values at the cell faces, as well as in secondary gradients for diffusion terms, pressure gradients for the pressure-velocity coupling, and strain-rate and rotation-rate calculations of the turbulence model. The discrete diffusion term is given by

$$\Gamma_f\nabla\phi_f\cdot\mathbf{a} = \Gamma_f[(\phi_1-\phi_0)\vec{\alpha}\cdot\mathbf{a} + \overline{\nabla\phi}\cdot\mathbf{a} - (\overline{\nabla\phi}\cdot\mathbf{ds})\boldsymbol{\alpha}\cdot\mathbf{a}] \ , \tag{36}$$

where $\mathbf{ds}$ is the differential vector that has the direction of the line that crosses the centroids of cells-0 and 1, $\boldsymbol{\alpha} = \mathbf{a}/(\mathbf{a}\cdot\mathbf{ds})$, $\overline{\nabla\phi} = (\nabla\phi_0 + \nabla\phi_1)/2$, and Γ_f is the harmonic average of cell diffusivity values. The algebraic system for the transported variable ϕ at iteration i+1 is expressed implicitly as

$$a_p\phi_p^{i+1} + \sum_n a_n\phi_n^{i+1} = b \ , \tag{37}$$

where the summation is over all the neighbors n of cell p. In the right-hand side, b represents the explicit contributions to the approximated equation and the coefficients a_p and a_n are obtained directly from the approximated terms. An under-relaxation factor ω is introduced implicitly as

$$a_p/\omega\, \phi_p^{i+1} + \sum_n a_n\phi_n^{i+1} = b + a_p/\omega\,(1-\omega)\phi_p^i \ , \tag{38}$$

where the superscript i+1 implies the value after the solution is produced, and the source term on the right-hand side evaluates at the previous iteration i. However, rather than solving Eq. (37) for the unknowns ϕ^{i+1}, the delta form

$$a_p/\omega\, \Delta\phi_p + \sum_n a_n \Delta\phi_n = b - a_p\phi_p^i - \sum_n a_n\phi_n^i \quad (39)$$

is used instead by defining $\Delta\phi_p = \Delta\phi_p^{i+1} - \phi_p^i$. The approximation approach described by the previous equations results in the linear system

$$\mathbf{Ax} = \mathbf{b} \quad (40)$$

which represents the algebraic equations for each cell. The matrix **A** represents the coefficients of the linear system (the coefficients a_p and a_n in the left-hand side of Eq. (39)), the vector **x** represents the unknowns in each cell ($\Delta\phi$ in the right-hand side of Eq. (39)), and the vector **b** represents the residuals (first term in the right-hand side of Eq. (39)). In order to solve Eq. (40), the authors adopt the CFD code Star-CCM+ (CD-adapco, 2013), which is setup to compute the pressure-velocity coupling of the flow using the SIMPLE algorithm (Patankar and Spalding, 1972), being the iteration scheme the Gauss-Seidel with under-relaxation of velocity, pressure, and turbulent viscosity.

3.2 Assessment of the numerical uncertainty

The estimation of the numerical uncertainty and grid independence of the results follows the generalized Richardson's Extrapolation Method (Roache, 1998). In this method, the asymptotic value ϕ_0 of a scalar ϕ is given by

$$\phi_0 \cong \phi_1 + (\phi_1 - \phi_2)/(r_{12}^{p_{obs}} - 1)\,, \quad (41)$$

where ϕ_1 and ϕ_2 are the values computed with the fine and coarse grids respectively, r_{12} is the refinement ratio between those grids, and p_{obs} is the observed order of convergence of the grid set. The refinement ratio r_{12} is given by

$$r_{12} = [(\text{fine grid cells})\,/(\text{coarse grid cells})]^{1/3}\,, \quad (42)$$

and the observed order of convergence is obtained by solving iteratively for p_{obs} the equation

$$\epsilon_{23}\%/(r_{23}^{p_{obs}} - 1) = r_{12}^{p_{obs}}[\epsilon_{12}\%/(r_{12}^{p_{obs}} - 1)]\,, \quad (43)$$

where the subscript "3" refers to the coarsest grid. In the previous equation, the Richardson Error Estimator is computed with

$$\epsilon_{n,\,n\text{-}1}\% = 100(\phi_n - \phi_{n\text{-}1})/\phi_{n\text{-}1}\,, \quad (44)$$

where n={1,2,3}. The grid convergence index of the fine grid is calculated with

$$GCI_{12}\% = F_S|\epsilon_{12}\%|/(r_{12}^{p_{obs}} - 1)\,, \quad (45)$$

where $F_S = 1.25$ is as a factor of safety over those quantities. The asymptotic value ϕ_0 is considered to be grid independent when $\alpha/r_{12}^{p_{obs}} \approx 1$, where $\alpha = GCI_{23}\%/GCI_{12}\%$.

3.3 Computational domain and grid generation

The topology of the computational domain matches the walls of a lid-driven cavity of square cross-section, and characteristic length $L_c = 1$ m. The spanwise aspect ratio (defined as the ratio between the width and length of the moving lid) is 0.5. The grids are generated following well-known guidelines (Mavriplis et al., 2009), which recommend three refinement levels for verification and numerical uncertainty estimation; two equally spaced cell layers adjacent to the walls; design grid refinement ratio $r_{ref} \cong \sqrt[3]{3}$; dimensionless near-wall distance $y_w^+ \equiv h_0 u_*/\nu \cong 1$, where h_0 is the height of the cell layer adjacent to the wall, $u_* = \sqrt{\tau_w/\rho}$ is the reference velocity, τ_w is the wall shear-stress and ν is the kinematic viscosity. The design value of y_w^+ dictates the height h_0 of the cell layer adjacent to the wall with

$$h_0 = 5.1988 y_w^+ L Re_L^{-0.9} \quad (46)$$

(Schlichting, 1979), and the cell layers away from the walls are distributed according to a one-parameter hyperbolic tangent stretching function. The (power-law) Reynolds number term in Eq. (46) is defined as

$$Re_L \equiv (\rho U_c^{(2-n)} L_c^n)/K\,, \quad (47)$$

and it gives the ratio of inertia and viscous fluxes for a given viscoplasticity. For the fluid and flow parameters into consideration where $Re_L \leq 50{,}000$ and $h_0 \cong$ 1E-4 m, the application of the previously mentioned guidelines yields the coarser grid with 221,184 cells, an intermediate (coarse) grid with 615,600 cells, and the fine grid with 1,859,000 cells where $r_{23} = 1.406 < r_{ref} < r_{12} = 1.445$.

3.4 Boundary conditions

The walls are considered to be non-slip, adiabatic, impermeable, and originating at the bottom, back-left corner of the cavity. The lid is positioned at $y = 1$ m, and it moves from left to right on the XZ plane at a constant characteristic velocity $\mathbf{U}_c$. This choice of boundary conditions gives rise to top-corner singularities, but those have virtually no effect over most of the flow field as their effects are confined to the neighborhood of the singular corners (Shankar and Deshpande, 2000).

3.5 Assessment of the inertia and viscoplasticity effects

In order to examine viscoplasticity and flow inertia effects separately, the authors follow the rationale discussed in dos Santos et al. (2011), in which the governing parameters are the power-law index n, the rheological Reynolds number

$$Re_r \equiv \rho\dot{\gamma}_1 L_c^2/\mu_1 \,, \tag{48}$$

where μ_1 is obtained by setting $\dot{\gamma} = \dot{\gamma}_1$ in Eq. (26), the dimensionless lid-velocity

$$U^* \equiv |\mathbf{U_c}|/\dot{\gamma}_1 L_c \,, \tag{49}$$

and the jump number

$$J \equiv (\dot{\gamma}_1 - \dot{\gamma}_0)/\dot{\gamma}_0 \,. \tag{50}$$

The rheological Reynolds number is interpreted as a dimensionless density based on the rheological properties of a fluid (dos Santos et al., 2011). In the situation in which $U^* \ll 1$, the fluid behaves as a high viscosity Newtonian fluid, and for $U^* \cong 1$ and higher values the fluid transitions to a power-law like controlled fluid. Therefore, U^* controls the yield stress effect, and it is interpreted as a dimensionless characteristic strain-rate. The jump number gives a measure of the strain-rate jump between the end of the Newtonian plateau at $\dot{\gamma}_0$, and the beginning of the power-law region at $\dot{\gamma}_1$. The lid-speed velocity $\mathbf{U}_c$ is set up such that the desired power-law Reynolds number is obtained for the n and K parameters.

3.6 Assessment of the state of turbulence

One can examine the anisotropy of the Reynolds stresses through the normalized anisotropy tensor **B**, defined by its components as

$$B_{ij} \equiv \overline{u_i' u_j'}/\overline{u_k' u_k'} - 1/3\delta_{ij} = A_{ij}/2k \,. \tag{51}$$

Tensor **B** has zero trace (i.e., $\mathrm{I_B} \equiv tr(\mathbf{B}) = B_{ii} = 0$), and consequently it has just two independent variants, $\mathrm{II_B} \equiv 1/2[-\mathrm{tr}(\mathbf{B}^2)]$ and $\mathrm{III_B} \equiv \det(\mathbf{B})$. By setting $6\eta^2 = -2\mathrm{II_B}$ and $6\xi^3 = 3\mathrm{III_B}$, the state of the anisotropy can be determined in terms of ξ and η at any point and time in a turbulent flow, and the result plotted in the ξ-η plane. The special states of the Reynolds-stress tensor that correspond to particular points in that plane, herein called the Lumley-Pope triangle (Lumley, 1978; Pope, 2000). Every Reynolds-stress that can occur in a turbulent flow has a matching point inside the Lumley-Pope triangle, and points outside correspond to Reynolds stresses having negative or complex eigenvalues (i.e., non-realizable turbulence). The isotropic state of turbulence ("iso") corresponds to the point where $\xi = \eta = 0$. The two-component, axisymmetric state ("2C, Axi") occurs when $\xi = -1/6$ and $\eta = 1/6$. For a channel flow, the one-component state of turbulence occurs where the dimensionless wall distance $y^+ \equiv y u_*/\nu \approx 7$. The axisymmetric state of turbulence ("Axi, $\xi > 0$" or "Axi, $\xi < 0$") occurs when $\xi = \eta$ (**B** has one large eigenvalue) or $\xi = -\eta$ (**B** has one small eigenvalue), and the two-component state of turbulence ("2C") characterizes in the situation where $\eta = (1/27 + 2\xi^3)^{1/3}$.

4. VERIFICATION AND VALIDATION

4.1 Simulation settings

The simulation settings are summarized in Tab. 1, where setting "A" and settings "C" to "E" applied to viscoplastic fluids, and settings "B" and "F" applied to Newtonian fluids. In addition, settings "A" and "B" applied to laminar flows (using $\mathbf{T} = \mathbf{T}_l$ in Eq. (2)), and settings "C" to "F" applied to turbulent flows (using the full set of equations of the mathematical model). The common rheological parameters of the viscoplastic fluids are J = 1E4, $\tau_0 = 1\ \mathrm{N/m^2}$, μ_0 = 1E4 $\mathrm{Pa \cdot s}$, and μ_{inf} = 1E-3 $\mathrm{Pa \cdot s}$.

Table 1. Flow and fluid settings of the simulation cases

Settings	A	B	C	D	E	F
U_c (m/s)	8.62E-3	8.89E-5	1.40E+1	1.81E+1	1.62E+1	4.44E-2
ρ (kg/m^3)	1250	1000	1000	1000	1000	1000
n	0.50	1.00	0.65	0.65	0.70	1.00
K (Pa $\cdot$ s^n)	1.00E+0	8.89E-4	1.25E+0	1.00E+0	7.50E-1	8.89E-4
Re	1	100	28200	50000	50000	50000
Re_r	625	-	250	500	1000	-
U^*	0.30	-	1.97	1.93	1.68	-
$\dot{\gamma}_0$ (s^{-1})	1.00E-4	-	1.00E-4	1.00E-4	9.33E-5	-
$\dot{\gamma}_1$ (s^{-1})	1.00	-	0.71	1.00	1.37	-
μ_1 (Pa $\cdot$ s)	2.00	-	2.82	2.00	1.37	-
$\dot{\gamma}_2$ (s^{-1})	1.00E+6	-	7.05E+8	3.73E+8	3.83E+9	-
$\dot{\gamma}_c$ (s^{-1})	0.01	-	14.00	18.13	16.25	-

4.2 Grid verification and numerical uncertainty analysis

The grid verification and numerical uncertainty analysis used settings "A" and "D" detailed in Tab. 1, and the wall shear-stress τ_w (the scalar in Eq. (41)) probed at the center of the bottom wall where $(x, y, z) = (0.50, 0.00, 0.125)$. The results are summarized in Tab. 2, where the $\alpha/r_{12}^{p_{obs}}$ values close to the unity indicate grid independency. The $GCI_{12}\%$ values for the fine grid range from 0.3% to 4.5%, such range considered adequate as the approximated solutions fall within an error band of 5% centered on the asymptotic value (Roache, 1998). Moreover, the observed order of convergence p^{obs} is approximately 2 as the approximations are second-order in space but first-order in time. Such results indicate that the fine grid shall produce accurate results within the range of Re_L values in Tab. 1.

Table 2. Summary of the numerical uncertainty analysis and grid independence of the results [a]

Setting	$\tau_{w,1}$	$\tau_{w,2}$	$\tau_{w,3}$	$\varepsilon_{23}\%$	$\varepsilon_{12}\%$	p^{obs}	$\tau_{w,0}$	$GCI_{23}\%$	$GCI_{12}\%$	$\alpha/r_{12}^{p_{obs}}$
A	0.2912	0.2904	0.2887	-0.5855	-0.2831	2.2751	0.2918	0.6237	0.2697	1.0050
E	53.1019	51.2956	48.2359	-5.9647	-3.4017	1.8063	55.0126	8.7497	4.4976	1.0039

[a] Subscripts "1", "2" and "3" correspond to the values obtained with the fine, coarse, and the coarsest grids respectively, and subscript "0" refers to the asymptotic value of τ_w ($\mathrm{N/m^2}$).

4.3 Validation of the numerical method

The validation of the numerical method used the simulation results of setting "B" for the fine grid, and the 2D cavity flow data from Guia et al. (1982) for $Re = 100$. For that purpose, the x component of the velocity profile (u) was probed alongside the vertical line that crosses the geometrical center of the cavity. The comparison results summarized in Tab. 3 show close agreement in the proximity of the bottom and top walls, and the discrepancies in the middle region of the 3D cavity are explained by the spanwise flows that do not exist in the 2D cavity simulations, as discussed in Shankar and Deshpande (2000). Although not shown here for the sake of brevity, the topology of the 3D velocity profile matches the results reported in Chiang et al. (1998) for that same Reynolds number, thus validating the numerical method.

Table 3. Validation of the results for $Re = 100$ (setting "B", results converged to the steady state)

y (m)	0.98	0.97	0.96	0.95	0.85	0.73	0.62	0.50	0.45	0.28	0.17	0.10	0.07	0.06	0.05
$u/\lvert\mathbf{U_c}\rvert$ [a]	0.80	0.74	0.68	0.62	0.10	-0.11	-0.18	-0.18	-0.17	-0.11	-0.07	-0.05	-0.04	-0.03	-0.03
$u/\lvert\mathbf{U_c}\rvert$ [b]	0.85	0.79	0.75	0.70	0.25	0.00	-0.13	-0.21	-0.21	-0.16	-0.10	-0.06	-0.04	-0.04	-0.03
$u/\lvert\mathbf{U_c}\rvert$ [c]	0.84	0.79	0.74	0.69	0.23	0.00	-0.14	-0.21	-0.21	-0.16	-0.10	-0.06	-0.05	-0.04	-0.04

[a] 3D Fine grid, where $(x, z) = (0.5, 0.25)$ m; [b] 2D Fine grid, where $x = 0.5$ m; [c] Guia et al. (1982)

The results for a laminar flow characterized by setting "A" in Tab. 1 are relevant in the interest of validation. With this purpose, Fig. 2a pictures the quasi-stagnant flow in the middle and cross-section planes, as well as the slow turning eddies at the bottom corners of the middle section. Such morphology matches the results reported in dos Santos et al. (2011) for $n = 0.5$, $Re_r = 0$, and U^* up to 0.25. In addition, Fig. 2b displays the middle-section cut of the unyielding region represented by the strain-rate iso-surfaces having $\dot{\gamma} \leq \tau_0/\mu_0 \leq$ 1E-4 s^{-1}. The topology of that region concurs with dos Santos et al. (2011) for simulations having $U^* = 0.01$, $n = 0.5$, and $Re_r \leq$ 5E3, and the results indicate the correct coupling of the SMD model and the numerical method.

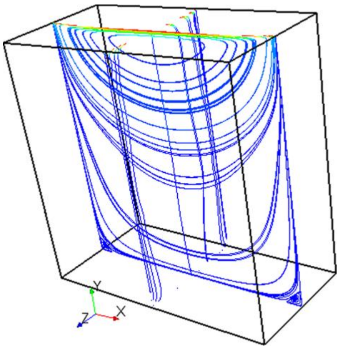

Figure 2a. Morphology of the streamlines, setting "A"

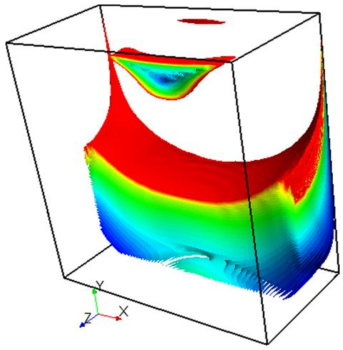

Figure 2b. Strain-rate iso-surfaces, setting "A"

5. RESULTS AND DISCUSSION

Setting "C" simulated as a turbulent flow, and the morphological features of the resulting flow were used to validate the more comprehensive analysis carried out using settings "D", "E" and "F". The first validation concerned the dimensionless near-wall distance y_w^+, expected to be near the unity per grid design. Alongside the flow-wise center line of the walls, $y_w^+ < 0.25$, except near the corners where the velocity gradients are higher and $y_w^+ \approx 2$. This result confirms the effectiveness of the low-Reynolds design of the grid.

In Fig. 3a, the morphology of the streamlines is examined in the middle and cross sections of the cavity, where one may observe a vortex eye developing from the center of the middle section, and secondary vortex eyes forming in the cross-section near the lid-wall. The lines defining the axes of the vortex cores are parallel to the edges of the cavity, thus indicating the presence of Taylor-Goertler vortices (Koseff and Street, 1984). In Fig. 3b, the cross-section of the velocity field of setting "C" is displayed, and one can identify some of the turbulent structures described in Kline and Robinson (1990), like the counter-rotating streamwise vortices near the top and bottom corners, the strong internal shear layers near the bottom corners, and ejections of low-speed fluid outward the bottom wall. The results of setting "C" are expected to repeat in simulations having higher Re_L, and therefore are not investigated for settings "D", "E" and "F".

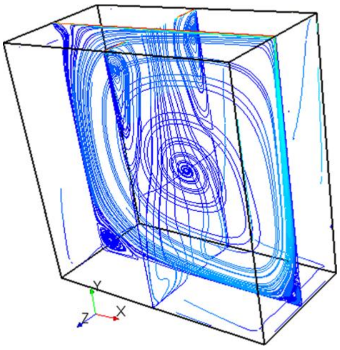

Figure 3a. Streamlines and vortex cores, setting "C"

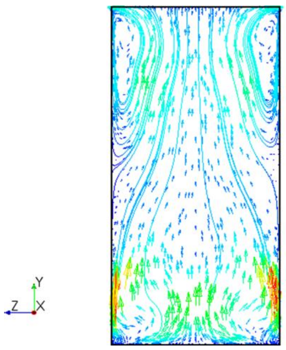

Figure 3b. Cross-section of the velocity field, setting "C"

In Fig. 4a, the dimensionless velocity profile $u^+ \equiv u/u_*$ is plotted against the dimensionless wall distance y^+ from the vertical wall at $x = 0.5$ m, alongside the horizontal line that crosses the middle-section of the cavity at $y/L_c = 0.5$, and in Fig. 4b the profiles are plotted alongside the vertical line that crosses the middle-section at $x/L_c = 0.5$ from the bottom wall at $y = 0$ m. One can observe that in the viscous sublayer ($y^+ \leq 5$) the law of the wall $u^+ = y^+$ holds regardless of the rheology of the fluid, and such result agrees with the computations in Cruz and Pinho (2003) for an inelastic shear-thinning fluid flow and $Re = 40000$. In the buffer layer and up to $y^+ \approx 10$, the profile also match the calculations of Cruz and Pinho (2003). In addition, the velocity profiles side with the experimental results of Escudier et al. (2009) for $Re = 42900$ of a 0.125% aqueous solution of polyacrylamide. For $y^+ > 10$, the velocity profiles are biased by the neighboring walls, and the inflection observed in the velocity profile of the viscoplastic fluids for $y^+ \approx 10$ occurs when the strain-rate reaches the value corresponding to the beginning of the power-law segment of the viscosity function, i.e., when $\dot{\gamma} \to \dot{\gamma}_1$.

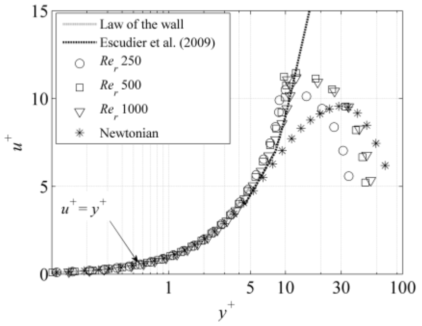

Figure 4a. Dimensionless velocity profiles at $y/L_c = 0.5$

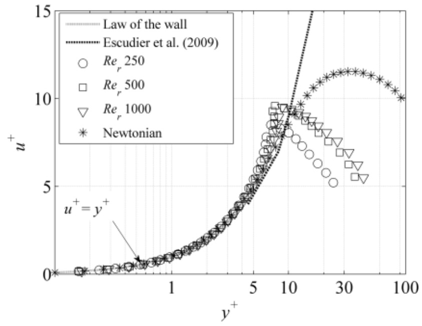

Figure 4b. Dimensionless velocity profiles at $x/L_c = 0.5$

Although the regularization of the viscosity function smoothly blends the power-law and the Newtonian plateau regions, when $\dot{\gamma} \to \dot{\gamma}_0$ the stresses may jump several orders of magnitude and destabilize the numerical solution. This observation suggests that mildly turbulent flows may be difficult or even impossible to compute in the strain-rate range where $\dot{\gamma}_0 \leq \dot{\gamma} \leq \dot{\gamma}_1$, and modifications should be considered in the transport equations if this situation cannot be avoided. Moreover, as the power-law index diminishes, the more unstable the numerical solution becomes, and the authors could not achieve converged results for power-law indexes $n < 0.5$. Therefore, a careful balance of fluid and flow settings should be selected when applying the mathematical model and the numerical method previously described, such that the characteristic strain-rate $\dot{\gamma}_c \equiv L_c/|\boldsymbol{U}_c| \gg \dot{\gamma}_1$. In Fig. 5a, one may observe wiggles due to the strain-rate fluctuations beyond the inner region, and in particular for $y^+ > 30$ the velocity profiles get biased by the spanwise flows and by the influence of the neighboring walls, eventually transitioning back to the velocity profile that matches the inner region of the diametrically opposite wall of that in consideration. In Fig. 5b, the plots of the SMD viscosity function of settings "C", "D", and "E" are compared against the respective computed values of the middle-section where $y/L_c = 0.5$, showing that the strain-rate values fall predominantly in the power-law region of the flow.

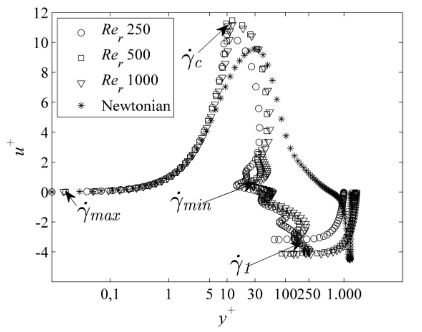

Figure 5a. Velocity profiles for $y/L_c = 0.5$

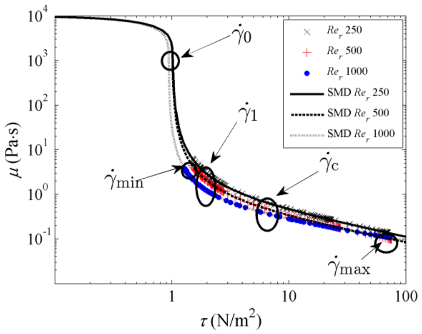

Figure 5b. Viscosity values for $y/L_c = 0.5$

The anisotropy of the Reynolds stresses in the middle-section can be qualitatively examined by mapping the special states of turbulence. For that purpose, Figures 6a, 6b, and 6c show those states of settings "D", "E" and "F" respectively. The inspection of those figures indicates the special states of turbulence have a similar pattern for the viscoplastic fluid flows (settings "D" and "E"), such result being expected as in both simulations $U^* > 1$ and the fluids have close rheology. However, the Newtonian fluid flow (setting "F") has a quite different state of turbulence pattern for the same flow inertia, showing that the fluid rheology does affect that state. For all settings in the near-wall region, the one-component and the two-component states of turbulence predominate, although for the viscoplastic fluid flows the two-component region stretches further away from the walls as compared with the Newtonian fluid flow. This behavior may be better understood by analyzing the Lumley-Pope plot of the anisotropy of the Reynolds stresses alongside the horizontal line that crosses the middle-section at $y/L_c = 0.5$, where the y distance measures from the right wall. In Figures 7a and 7b, the turbulence evolves from the one-component state ($u'^2_j = u'^2_k = 0$) to the two-component state ($u'^2_j = 0$) in the region where $y^+ < 10$, where the trajectory sharply turns towards the two-component axisymmetric contraction state ($\xi > 0$, with $u'^2_i > u'^2_j = u'^2_k$). In the range where $10 \leq y^+ < 30$ (i.e., the buffer-layer segment of the inner region of the velocity profile) the turbulence has mixed states, and for $y^+ > 30$ the state of turbulence fluctuates between the axisymmetric contraction and axisymmetric expansion ($\xi < 0$, with $u'^2_i > u'^2_j = u'^2_k$). The region where $y^+ > 300$ is mostly influenced by the opposite wall (i.e., the left wall). In Fig. 7c, the return-to-isotropy trajectory of the Newtonian fluid flow (setting "F") is examined, and it shows a general behavior in agreement with DNS of channel flow reported in Moser et al. (1999). However, the comparison of the return-to-isotropy trajectories in the near-wall region of the viscoplastic fluid flows against that of the Newtonian fluid flow shows the anisotropy (i.e., the value of η) is higher in the former than in the latter fluid flow. Moreover, for $y^+ > 100$ the state of turbulence remains axisymmetric contraction, as opposed to those of the viscoplastic fluid flows that show fluctuation between the axisymmetric contraction and expansion states.

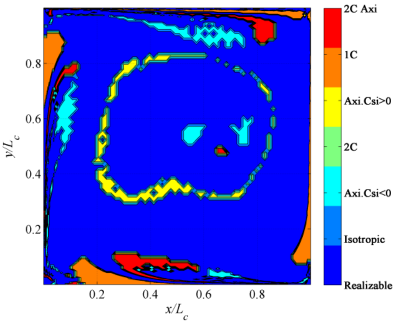

Figure 6a. Special states of the turbulence, setting "D"

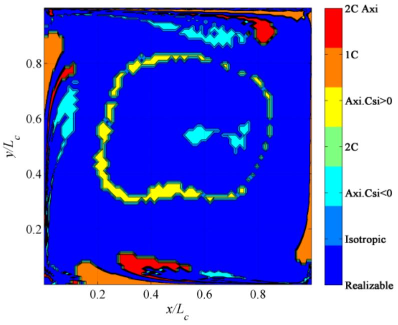

Figure 6b. Special states of the turbulence, setting "E"

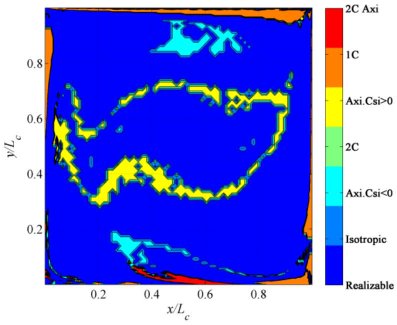

Figure 6c. States of the turbulence, setting "F"

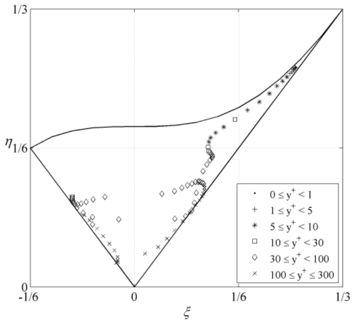

Figure 7a. Return-to-isotropy trajectory, setting "D"

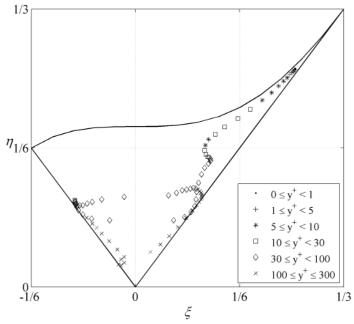

Figure 7b. Return-to-isotropy trajectory, setting "E"

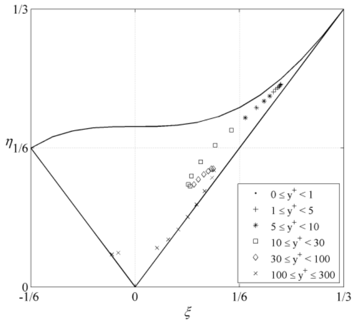

Figure 7c. Return-to-isotropy trajectory, setting "F"

6. CONCLUSIONS

The authors adopted a numerical method to simulate the turbulent 3D lid-driven cavity flow of viscoplastic fluids, in order to validate the application of the linear pressure-strain Reynolds Stress Transport turbulence model to solving flow quantities of those fluids. For that use, the SMD model provided a regularized viscosity function, and the Navier-Stokes transport equations coupled with the turbulence model. The Finite-Volume method approximated the transport equations, and the CFD code STAR-CCM+ solved the system of approximated equations. The design of the grids followed best practices to allowing verification and validation. The assessment of the viscoplasticity and inertia effects used dimensionless flow and rheological quantities, and the analysis of the state of turbulence relied on the mapping of the anisotropy of the Reynolds stresses. After verifying the set of grids and validating the numerical method, the authors discussed the effects of the flow inertia and the fluid rheology on the morphology of the flows. For a range of increasing the Reynolds numbers, the authors discussed the combined effects of inertia and fluid rheology on the state of turbulence, and also established parallels with that of a Newtonian fluid flow. For a mildly turbulent flow, the authors investigated the morphology of the turbulent structures like vortices, ejections and spanwise flows, and concluded that those structures indeed confirm the flows as turbulent. Moreover, the inspection of the velocity profiles agreed with experimental and numerical data, and consideration were drawn concerning the applicability and stability of the numerical solution in the limiting case of strong non-linearity of the viscosity function. After inspecting the velocity profiles the authors discussed the state of turbulence of the flows, and showed that the rheology of the fluids markedly influences the state of turbulence, as well as the return-to-isotropy trajectories of the Reynolds stresses. In summary, the results presented are consistent from both the rheological and turbulence phenomena perspectives. Further, the mathematical formulation and the numerical method successfully combined the linear pressure-strain Reynolds Stress Tensor turbulence model and the SMD model, being such strategy applicable for other regularized (smooth) viscosity functions, moderate power-law indexes, and having the strain-rate range within the power-law controlled segment of the viscosity function.

7. ACKNOWLEDGEMENTS

The authors thank the financial support from CAPES, through a doctor scholarship grant for Beck, P.A, and from CNPq, through scientific productivity grants for Vielmo, H.A. and Frey, S.L, and the CNPq Universal Project 470325/2011-9.

8. REFERENCES

Bird, R.B., Dai, G.C. and Yarusso, B.J., 1982. “The rheology and flow of viscoplastic materials”. *Rev. Chem. Eng.*, Vol. 1, pp. 1-70.

CD-adapco, 2013. *STAR-CCM+ Version 8.06*. User’s Guide.

Chiang, T.P. Sheu, W.H. and Hwang, R.R., 1998. “Effect of Reynolds number on the eddy structure in a lid-driven cavity”, *Int. J. Numer. Meth. Fluids*. Vol. 26, pp. 557–579.

Cruz, D.O.A, Maneschy, C.E., Macedo, E.N. and Quaresma J.N.N., 2000. “A turbulence model for computing the flow of power law fluids within circular tubes”. *Hybrid Meth. Eng*. Vol. 2, pp. 1-13.

Cruz, D.O.A. and Pinho, F.T., 2003. “Turbulent pipe flow predictions with a low Reynolds number $k-\varepsilon$ model for drag reducing fluids”, *J Non-Newton. Fluid*. Vol. 114, pp. 109-148.

de Souza Mendes, P.R, 2007. “Dimensionless viscoplastic Fluid Mechanics”. *J. Viscoplastic Fluid Mech*. Vol. 147, pp. 109-116.

de Souza Mendes, P.R. and Dutra, E.S.S., 2004. “Viscosity Function for Yield Stress Liquids”, *App. Rheol.* Vol. 14 pp 296-302.

dos Santos, D.D., Frey, S.L., Naccache, M.F. and de Souza Mendes P.R., 2011. “Numerical approximations for flow of viscoplastic fluids in a lid-driven cavity”. *J. Viscoplastic Fluid. Mech*. Vol. 166, pp. 667-679.

Escudier, M.P., Nickson, A.K. and Poole, R.J., 2009. “Turbulent flow of viscoelastic shear-thinning liquids through a rectangular duct: Quantification of turbulence anisotropy”. *J Non-Newton Fluid*. Vol. 160, pp. 2–10.

Ghia, U., Ghia, K.N. and Shin, C.T., 1982. “High-Re Solutions for Incompressible Flows Using the Navier-Stokes Equations and Multigrid Methods”. *J. Comput. Phys.*, Vol. 48, pp. 387-411.

Gibson, M.M. and Launder, B.E., 1978. “Ground effects on pressure fluctuations in the atmospheric boundary layer”. *J. Fluid Mech*. Vol. 86, pp. 491-511.

Gori, F. and Boghi, A., 2012. “Three dimensional exact equation for the turbulent dissipation rate of Generalised Newtonian Fluids”. *Int. Comm. Heat Mass Transfer*. Vol. 39, pp. 477–485.

Huigol, R.R. and Hou, Z., 2005. “Application of the augmented Lagrangian method to steady pipe flows of Bingham, Casson and Herschel-Bulkley fluids”. *J. Viscoplastic Fluid Mech*. Vol. 128, pp. 126-143.

Kline, S.J. and Robinson, S.K., 1990. “Quasi-coherent Structures in the Turbulent Boundary Layer: Part I. Status Report on a Community-Wide Summary of the Data”. In *S.J. Kline and N.H. Afgan (Eds.), Near-wall Turbulence.* NY, Hemisphere.

Koseff, J.R. and Street, R.L., 1984. “Visualization of a shear driven three-dimensional recirculating flow”. *J. Fluids Eng*. Vol. 106, pp. 21-29.

Launder, B.E., Reece, G.J. and Rodi, W., 1975. “Progress in the development of a Reynolds-stress turbulence closure”. *J. Fluid. Mech*. Vol. 68, pp. 537-566.

Lumley, J.L., 1978. “Computational Modeling of Turbulent Flows”. *Advances in Applied Mechanics*. Vol. 18, pp. 123-176.

Malin, M.R., 1997. “Turbulent Pipe Flow of Power-Law Fluids”. *Int. Comm. Heat Mass Transfer*. Vol. 24, pp. 977-988.

Malin, M.R., 1998. “Turbulent Pipe-Flows of Herchel-Bulkley Fluids”. *Int. Comm. Heat Mass Transfer*. Vol. 25, pp. 321-330.

Mavriplis, D.J., Vassberg, J.C., Tinoco, E.N., Mani, M., Brodersen, O.P., Eisfeld, B., Wahls, R.A., Morrison, J.H., Zickuhr, T., Levy, D. and Murayama M., 2009. “Grid Quality and Resolution Issues from the Drag Prediction Workshop Series”. *J. Aircraft.* Vol. 46, pp. 935-950.

Moser, R.D., Kim, J. and Mansour, N.N., 1999. “Direct numerical simulation of turbulent channel flow up to $Re_\tau = 590$”, *Physics of Fluids*, Vol. 11, pp. 943-945.

Patankar, S.V., 1980. *Numerical Heat Transfer and Fluid Flow*. Taylor & Francis Group LLC, NY.

Patankar, S.V. and Spalding, D.B., 1972. “A Calculation Procedure for Heat, Mass and Momentum Transfer in Three-Dimensional Parabolic Flows”, *Int. J. Heat. Mass Tran.* Vol. 15, pp. 1787-1806.

Peixinho J., Nouara, C., Desaubrya, C. and Théron, B., 2005. “Laminar transitional and turbulent flow of yield stress fluid in a pipe”. *J. Viscoplastic Fluid Mech*. Vol. 128, pp. 172-184.

Pope, S.B., 2000. *Turbulent Flows*. Cambridge University Press, UK.

Schlichting, H., 1979. *Boundary Layer Theory seventh ed.* McGraw-Hill Book Company, New York.

Shankar, P.N. and Deshpande, M.D., 2000. “Fluid Mechanics in the Driven Cavity”. *Annu. Rev. Fluid Mech*. Vol. 32 pp. 93–136.

Roache, P.J., 1998. *Verification and Validation in Computational Science and Engineering*. Hermosa Publishers, Albuquerque.

Rodi, W., 1991. “Experience with Two-Layer Models Combining the k- ε Model with a One-Equation Model Near the Wall”. In *29th Aerospace Sciences Meeting, January 7-10, Reno, NV, AIAA Paper 91-0216*.

Rudman, M. and Blackburn, H.M., 2006. “Direct numerical simulation of turbulent viscoplastic flow using a spectral element method”. *Appl Math Model*. Vol. 30, pp. 1229-1248.

Wolfstein, M., 1969. “The velocity and temperature distribution in one-dimensional flow with turbulence augmentation and pressure gradient”. *Int. J. Heat Mass Transfer*. Vol. 12, pp. 301-318.

Venkatakrishnan, V., 1993. “On the Convergence of Limiters and Convergence to Steady State Solutions”. *AIAA Paper 93-0880*.

9. RESPONSIBILITY NOTICE

The authors are the only responsible for the printed material included in this paper.